Water Resources Research

RESEARCH ARTICLE
10.1029/2019WR025381

Wettability Effects on Primary Drainage Mechanisms and NAPL Distribution: A Pore-Scale Study

Ian L. Molnar[1,2], Jason I. Gerhard[1], Clinton S. Willson[3], and Denis M. O'Carroll[1,4]

[1]Department of Civil and Environmental Engineering, The University of Western Ontario, London, ON, Canada, [2]Now at Grant Institute, School of Geosciences, University of Edinburgh, Edinburgh, UK, [3]Now at School of Civil and Environmental Engineering, Connected Water Initiative, University of New South Wales, Sydney, NSW, Australia, [4]Department of Civil and Environmental Engineering, Louisiana State University, Baton Rouge, LA, USA

Key Points:
- Water drainage in intermediate wetting system deviated from expected percolation behavior
- Intermediate wetting pores are completely NAPL-filled upon drainage and exhibit no film drainage
- NAPL bypassed larger pores more frequently in intermediate wetting sand than in water wetting sand, leaving multipore water residual ganglia

Supporting Information:
- Supporting Information S1

Correspondence to:
I. L. Molnar,
ian.molnar@ed.ac.uk

Citation:
Molnar, I. L., Gerhard, J. I., Willson, C. S., & O'Carroll, D. M. (2020). Wettability Effects on Primary Drainage Mechanisms and NAPL Distribution: A Pore-Scale Study. *Water Resources Research*, *56*, e2019WR025381. https://doi.org/10.1029/2019WR025381

Received 22 APR 2019
Accepted 10 NOV 2019
Accepted article online 15 NOV 2019

Abstract The pore-scale processes governing water drainage behavior in porous media have implications for geoscience multiphase scenarios including carbon capture and storage, contaminant site remediation, oil recovery, and vadose zone processes. However, few studies report directly observed pore-scale water drainage phenomena in 3-D soils. This knowledge gap limits our ability to verify assumptions underlying existing models and develop optimal solutions. This paper utilizes synchrotron X-ray microtomography to present an experimental pore-scale examination of nonaqueous phase liquid (NAPL)/water distribution along a primary drainage front as dense NAPL was injected upward into water wetting (WW) and intermediate wetting (IW) sand-packed columns. Pore-network structures were extracted from imaged data sets and mapped onto segmented NAPL/water data sets which allowed quantitative examinations of wettability impacts on (a) the extent to which NAPL fills individual pore bodies and (b) relationships between pore size and the phase occupying the pore, with both considered as a function of distance (and capillary pressure) relative to the NAPL front. These results revealed that several hypotheses treating IW sand similarly to WW sands are simplistic. IW systems exhibited a sequence of pore filling that deviated from traditional capillary pressure-based model predictions: NAPL invades smaller pores, while larger, adjacent pores are bypassed leaving multipore residual water ganglia. NAPL pore saturations were close to 1 and did not change with capillary pressure in IW systems. Overall, the results illustrate how a relatively small change in operative contact angle alters NAPL distribution during water drainage, with important implications for geoscience multiphase flow scenarios.

1. Introduction

Research into the processes governing multiphase flow is driven by the many relevant applications in groundwater science and engineering. These include 1) carbon capture and storage systems, 2) groundwater susceptibility to colloid contamination (e.g., viruses or pathogenic bacteria within applied manure), 3) subsurface water balance (e.g., estimating evapotranspiration rates), and 4) remediation technologies and risk assessments for subsurface contamination by nonaqueous phase liquids (NAPLs).

Multiphase flow applications are strongly impacted by water drainage processes. Carbon capture and storage (CCS) systems are expected to continuously operate over a period of decades (Gershenzon et al., 2017) during which CO_2 displacement of water will dominate. The distribution of pore-scale capillary fringe structures associated with falling groundwater tables (e.g., thin water films, air/water interfaces, and pendular rings) impacts the migration of colloids and the rate of subsurface water evaporation (Flury & Qiu, 2008; Han et al., 2006; Norouzi Rad et al., 2013; Shahraeeni & Or, 2010; Shokri et al., 2008; Sirivithayapakorn & Keller, 2003; Wan & Tokunaga, 1997). The factors governing the remediation and lifespan of dense NAPL (DNAPL)-contaminated sites, such as the ganglia to pool ratio (Lemke & Abriola, 2006), DNAPL/water surface area (Bradford & Abriola, 2001; Chomsurin & Werth, 2003), and relative permeability (Nambi & Powers, 2000; Powers et al., 1998) are dependent upon NAPL invasion/migration/redistribution.

The development of X-ray computed microtomographic (XCT) imaging techniques has enabled many recent studies to examine the pore-scale processes governing multiphase flow in natural soils. These XCT studies have focused largely on water imbibition (i.e., the displacement of nonaqueous fluids by water) and the subsequent distribution of nonaqueous fluid residual [e.g., Al-Raoush et al., 2003; Al-Raoush & Willson, 2005a;

Schnaar & Brusseau, 2005; Han et al., 2006; Schnaar & Brusseau, 2006; Al-Raoush, 2009; Kumar et al., 2010; Iglauer et al., 2011; Iglauer et al., 2012; Kumar et al., 2012; Andrew et al., 2013; Chaudhary et al., 2013; Andrew et al., 2014a, 2014b, 2014c; Geistlinger et al., 2014; Geistlinger & Mohammadian, 2015; Rücker et al., 2015; Al-Menhali et al., 2016; Singh et al., 2016]. In contrast, few experimental XCT studies are available on pore-scale water drainage (i.e., the displacement of water by nonaqueous fluids) within natural soils (Andrew et al., 2015; Berg et al., 2013; Bultreys et al., 2015; Culligan et al., 2006; Herring et al., 2013; Herring et al., 2015; Herring et al., 2016; Porter et al., 2010; Wildenschild et al., 2005).

These experimental water drainage XCT studies have yielded valuable insights into the pore-scale processes driving water drainage, extending our understanding of these processes beyond the initial 2-D micromodel studies exploring capillary and viscous fingering (e.g., Lenormand et al., 1983; Lenormand et al., 1988). The existence of Haines jumps in 3-D media has since been examined using real-time XCT imaging (Berg et al., 2013; Bultreys et al., 2015). Wildenschild et al. (2005) employed XCT to illustrate how large, well-connected pores drain first. Other XCT studies have examined nonaqueous fluid/water interfacial areas during drainage (Culligan et al., 2006; Porter et al., 2010) as well as how drainage processes can yield small-scale snap-off events (Andrew, Menke, et al., 2015). Pore-scale XCT studies have explicitly linked the distribution of NAPL following drainage with trapping efficiency in CCS systems (Herring et al., 2013; Herring et al., 2015; Herring et al., 2016) showing that hydrophobicity increases the connectivity of the nonaqueous fluid phase and reduces trapping. These XCT studies have been complemented by pore-network modeling which has identified additional water drainage mechanisms such as cooperative pore filling (Holtzman & Segre, 2015; Zhao et al., 2016). However, a majority of these studies employed systems where water was strongly wetting with respect to the nonaqueous phase; knowledge gaps still exist for drainage in which nonideal wetting dominates.

Wettability significantly affects water drainage and imbibition behavior. Wettability is the preferential spreading of a fluid over a solid surface in the presence of another fluid (Anderson, 1986b; Powers et al., 1996) and is quantified by the contact angle formed at the fluid/fluid/solid interface. In this study, contact angle refers to the angle measured through the water phase on a flat surface where $0° < \theta < ~60°$ indicates water wetting (WW) systems, $~60° < \theta < ~120°$ indicates intermediate wetting (IW) systems, in which the solid surface has no strong preference for either fluid, and $~120° < \theta < 180°$ indicates NAPL-wetting (NW) systems (Anderson, 1986a; Powers et al., 1996). In addition, porous media may also possess "mixed wettability," which refers to media whose surfaces possess a range of wetting conditions (Anderson, 1987b).

Wettability is important in the multiphase applications under discussion. Many of the experimental studies exploring pore-scale water drainage processes employed WW media, assuming this was representative of the subsurface. However, numerous studies have illustrated the wide range of scenarios in which the subsurface may be rendered IW. CCS systems may employ oil-reservoir rocks with altered wettability (e.g., Chaudhary et al., 2013; Iglauer et al., 2015) or the injected CO_2 may render reservoirs IW or weakly WW (Arif et al., 2016; Arif et al., 2017; Bikkina, 2011; Broseta et al., 2012; Chiquet et al., 2007). Naturally occurring organic constituents in the subsurface may render the capillary fringe IW (Shokri et al., 2009; Ustohal et al., 1998). The wettability of near-surface soils has been modified by forest fires (Beatty & Smith, 2010). NAPL contaminants at brownfield sites may experience a range of wetting conditions due to either additives within the NAPL (e.g., surfactants and antioxidants) (Hsu & Demond, 2007; Lord, 1999) or organic components within the subsurface (Ryder & Demond, 2008). Enhanced oil recovery techniques improve microscopic sweep efficiencies (i.e., pore-scale oil displacement) by injecting surfactants to deliberately manipulate oil/water/mineral capillary forces (e.g., Kamal et al., 2017) and have noted optimal recovery rates under IW scenarios (Hou et al., 2016; Jadhunandan & Morrow, 1995; Kennedy et al., 1955; Morrow, 1990). In addition, pore-network modeling studies have employed the concept of mixed wettability (either naturally occurring or deliberately altered via injected surfactants) to describe behavior observed during waterflooding for oil recovery (e.g., Blunt, 1998; Blunt et al., 2002; Dixit et al., 2000; Kovscek et al., 1993; Oren et al., 1998; Oren & Bakke, 2003).

The standard conceptual model of quasistatic water (primary) drainage in WW media generally consists of two dominant pore-body drainage mechanisms: (1) Piston drainage, once an individual pore's displacement pressure (P_d) is exceeded by the local capillary pressure (P_c), nonaqueous fluid rapidly displaces the bulk wetting fluid (Haines, 1930; Lenormand, 1986; Melrose & Brandner, 1974) (i.e., "Haines jumps"), starting

with the largest pore throats (lowest P_d); (2) Film drainage, in which the remaining water surface films, near grain-grain contacts and in small throats, slowly drains via film connections to the bulk wetting phase (Salathiel, 1973).

Altered wettability changes the mechanisms driving water drainage. Generally, water drainage occurs at much lower capillary pressures in IW systems because larger contact angles decrease the curvature needed for NAPL to invade a pore throat (Anderson, 1987b; Morrow, 1976). This suggests that for a given P_c, smaller pores will be invaded in altered wetting systems versus WW. In strongly NW systems, nonaqueous fluid spontaneously imbibes into pores via films draining the smallest pores first, leaving water residual in the centers of the largest pores (Anderson, 1987a). However, in IW systems, the films are less likely to exist, and the inter- and intrapore drainage behavior is less straightforward than in either strongly WW or NW scenarios (Herring et al., 2016). The disruption of water films in altered wetting media reduces film straining, an important colloid retention mechanism in unsaturated systems, increasing colloid transport (Han et al., 2006; Wan & Tokunaga, 1997). Geologic reservoirs that are either IW or NW will possess lower carbon trapping efficiencies than WW reservoirs (Al-Menhali et al., 2016; Al-Menhali & Krevor, 2016; Alyafei & Blunt, 2016; Broseta et al., 2012; Chaudhary et al., 2013; Chiquet et al., 2007; Iglauer et al., 2012; Krevor et al., 2012; Krevor et al., 2015; Pentland et al., 2011).

Current understanding of these drainage mechanisms arises largely from a mixture of theoretical (i.e., mathematical) studies, bench-scale observations, 2-D etched-channel micromodels, modelling, and the few XCT studies mentioned previously. There is little experimental data of directly observed pore-scale water drainage processes in 3-D porous media; much of the directly observed pore-scale drainage phenomena are from 2-D micromodels (e.g., Lenormand, 1986; Lenormand et al., 1983; Lenormand et al., 1988) with relatively simplistic pore networks and drainage pathways. Key water drainage phenomena identified from 2-D micro model experiments have not been investigated for 3-D networks, limiting the ability to directly verify their findings for 3-D media and to accurately describe water drainage behavior in complex multiphase applications in 3-D networks representative of natural soils.

The pore drainage order has been indirectly examined in micromodel and XCT studies by comparing the distribution of residual nonaqueous fluids following water reimbibition to predictions from percolation theory. Percolation Theory is a mathematical theory describing the pore-scale distribution of fluids during drainage and imbibition (Adler & Brenner, 1988; Berkowitz & Ewing, 1998; Heiba et al., 1986; Wilkinson & Willemsen, 1983) by mimicking the classic pore drainage order; the invading fluid advances through the medium by invading the most favorable pore/throat at the fluid/fluid interface (i.e., the pore/throat with the lowest capillary pressure threshold) (Wilkinson & Willemsen, 1983). One consequence of this fluid displacement behavior is that percolation theory predicts a power-law distribution of residual ganglia sizes (Wilkinson & Willemsen, 1983); this prediction has been examined by numerous XCT and micromodel pore-scale studies during imbibition (e.g., Andrew et al., 2015; Geistlinger et al., 2015; Geistlinger & Ataei-Dadavi, 2015; Geistlinger & Mohammadian, 2015; Georgiadis et al., 2013; Iglauer et al., 2011; Iglauer et al., 2012) and water drainage (Georgiadis et al., 2013). While these studies revealed key information about the pore-scale behavior of multiphase-porous media systems, they only indirectly examined pore invasion order, whether due to imbibition or drainage processes.

Pore-network modeling is similar to percolation theory in concept but with added layers of sophistication. Whereas percolation theory models typically assume that a pore is either fully saturated with water or NAPL, pore-network models typically calculate the NAPL pore saturation (i.e., the fraction of a pore body's volume occupied by NAPL) of an invaded pore based on the radius of curvature from the system's capillary pressure (e.g., Blunt, 1998; Blunt et al., 2002; Oren et al., 1998; Oren & Bakke, 2003). That approach predicts a minimum NAPL pore saturation which depends upon the pore body's geometry (Blunt et al., 2002; Joekar-Niasar & Hassanizadeh, 2012) which to the best of the authors' knowledge has never been quantified by experimental observations despite the impact that pore geometry and pore-body saturations have on simulation outcomes.

Key knowledge gaps remain in the understanding of multiphase flow through porous media, limiting our ability to ensure optimal outcomes for subsurface multiphase applications. Pore-scale water drainage behaviors are not well understood as most studies have focused on examining residual fluid distributions. Pore-scale water drainage under weakly WW and IW conditions specifically are poorly understood as they have

Table 1
Overview of PCE/Water/Surface Contact Angles[a]

Parameter	WW sand	IW sand
Surface type	Iron oxide	Quartz
Smooth plate contact angle (°)[b]	25	160
Operative contact angle (°)[b,c]	<1	63

[a]From Molnar et al. (2011) [b]Reported through water phase during NAPL advancement/water drainage [c]Determined by Leverett-scaling capillary pressure-saturation relationships

received little attention in the literature (Herring et al., 2016). There have been no studies quantifying the NAPL pore saturations produced by Haines jumps and how wettability impacts those saturations. In addition, there have been no studies directly quantifying the pore drainage order for either WW or weakly water/IW scenarios and comparing that to theoretical predictions. Direct observations and quantification of these drainage mechanisms will lead to improved descriptions of pore-scale water drainage mechanisms in pore-network and continuum-scale models, improving outcomes for subsurface multiphase applications.

The goal of this study was to improve our conceptual understanding of multiphase flow through soil by filling the knowledge gaps identified above with direct pore-scale, experimental observations of water drainage in WW and IW sands. Synchrotron X-ray computed microtomography (SXCMT) was employed to collect images of NAPL and water distribution during water drainage from two sand-packed columns, one WW and the other IW. This study examined how WW and IW conditions (a) impacted NAPL pore saturations and (b) impacted the relationship between pore size and pore phase occupancy (i.e., the pore is dominated by either NAPL or water). The results reveal how shifting from WW to IW conditions leads to results that deviate from predictions of percolation theory.

2. Materials and Methods

2.1. Materials

The chemical samples employed in this study, and their method of preparation, followed the procedure described in Molnar et al. (2011). A NAPL/water/surfactant mixture was created in the wet lab in the GeoSoilEnviro Center for Advanced Radiation Sources at Argonne National Lab's Advanced Photon Source approximately 24 hr prior to scheduled beam time. Deionized Ultra-Filtered Water (Fisher Scientific) was employed as the aqueous phase. The NAPL used throughout this study was tetrachloroethylene (PCE) (Alfa Aesar, 99%) dyed with 0.25 g/L Oil-Blue-N (Sigma-Aldrich, 96%). The surfactant used to alter the sands' wettability, dodecylamine (Alfa Aesar, 98 + %), was added directly to the PCE at 3.5 g/L. Dodecylamine in PCE renders quartz sand's IW while leaving iron oxide-coated sands WW at pH values above 6 (Molnar et al., 2011). The PCE was doped with 1-Iodononane (Alfa Aesar, 97%) at 8% by volume to enhance its contrast with water during SXCMT imaging without substantially changing the wetting properties of the system. A closed glass bottle containing a 1:6.3 PCE:water volumetric ratio was titrated with hydrochloric acid (Fisher Scientific, ACS Grade) to control pH and was allowed to equilibrate on a shaker table for 24 hr. Separate mixtures were created for the quartz and iron oxide drainage experiments; as a result, their pH values vary slightly (quartz mixture: 6.8, iron oxide mixture: 6.7), but not enough to substantially impact their chemical or surface properties. All glassware was thoroughly cleaned using previously described methods (Molnar et al., 2011).

The sand employed in this study was a 40/50 Accusand mixture (Unimin, diameter: 300–420 μm). The sand was initially acid washed following the procedure of Molnar et al. (2011). Approximately, half of the sand was set aside as-is for use as an IW quartz sand, while the other half was coated with an iron oxide surface coating using the method of Johnson et al. (1996), also used by Molnar et al. (2011), so that it would remain WW in the presence of dodecylamine.

The NAPL/water/soil systems examined in this study were chosen to reproduce the wetting conditions quantified by Molnar et al. (2011) who measured NAPL/water/solid contact angles for these systems on smooth plates and packed columns of quartz and iron oxide sands (see Table 1). The PCE/DDA samples in that study rendered smooth quartz surfaces strongly NL, while smooth iron oxide surfaces remained strongly WW. Packed iron oxide sand columns remained strongly WW for iron oxide and but became IW for quartz sand. Throughout this paper, we refer to the NAPL/water/quartz sand system as “IW Sand” and the NAPL/water/iron oxide sand system as “WW Sand.”

The study presented here assumes that the wetting conditions quantified by Molnar et al. (2011) remain directly applicable and are uniform throughout both quartz and iron oxide sands. Johnson et al. (1996) reported that the iron oxide coating procedure—the same procedure employed in this study—resulted in

a uniform iron oxide coating over the grain surface. It is assumed that the uniform grain coating yields a homogenous wetting condition throughout the iron oxide sand.

2.2. Column Experiments

The sands were wet-packed into two small aluminum columns (ID: 5.6 mm, length: 5 cm). One column contained quartz sand, while the other contained iron oxide-coated sand (referred to throughout this study as IW sand and WW sand, respectively). Water from the water/PCE/surfactant mixture was flushed through each column for at least 20 pore volumes to allow the sand and surfactant to reach equilibrium. Following flushing, the water-saturated columns were securely mounted in the imaging hutch. The PCE mixture was injected upward using a syringe pump into the column at 200 μL/min, and water was allowed to freely exit the top of the column. The objective was to create NAPL distributions of approximately the same height in the two columns for comparison. The quartz column was imaged at cumulative injected PCE volumes of 100, 150, 300, and 400 μL, and the iron oxide column was imaged at 100, 150, and 200 μL. These volumes were chosen to yield similar NAPL heights within the columns. The pressure drops during DDA flushing and NAPL injection were not measured. The potential influence of dynamic effects on the NAPL distribution within the columns were estimated by calculating $\tau_s \frac{\partial S_w}{\partial t}$ where τ_s is the damping coefficient estimated from Stauffer (1978) (3.5×10^3 kg/m/s) and $\frac{\partial S_w}{\partial t}$ is the column-averaged rate of saturation change (<0.01 s^{-1}). Given the small $\tau_s \frac{\partial S_w}{\partial t}$ values (~23 Pa), it is assumed that dynamic effects did not influence the macroscopic drainage behavior of the WW and IW columns.

2.3. Imaging, Reconstruction, and Segmentation

Imaging for this study was conducted at the GSECARS 13BM-D imaging beamline. Imaging was performed above and below the iodine K-edge at 33.27 and 33.07 keV so that image subtraction could isolate the iodine-doped NAPL. During imaging, the column was rotated 180° while capturing 720 projections at each energy. The image resolution was 10.58 μm/pixel for the quartz experiment and 10.46 μm/pixel for the iron oxide experiment. After each flow stoppage, images were collected along 20 mm of the column with a 50 pixel overlap so that the reconstructed data sets from each time step could be stitched together to create a continuous 3-D data set of NAPL/water distribution along the entire front. Representative vertical cross sections of all collected and reconstructed data sets are presented in the supplementary information. Approximately 45–60 min elapsed during each injection and imaging time step.

It is assumed in this study that exposure to X-ray radiation during the imaging process did not alter the wetting behavior in either system. Brown et al. (2014) noted that X-ray radiation could alter the wetting behavior in three-phase systems through a hypothesized interaction between oil spreading along air/water interfaces and X-ray exposure. The two-phase systems examined here do not possess those three fluid-phase interfaces that led to X-ray wetting alterations. In addition, qualitative examination of the time-lapse images in Figures S1 and S2 indicates that the wetting behaviors do not change over time (i.e., with further exposure to X-rays). Previous two-phase XCT studies do not discuss X-ray-induced wetting alterations (e.g., Al-Raoush, 2009; Andrew et al., 2014a, 2014b, 2014c; Chaudhary et al., 2013; Culligan et al., 2006; Han et al., 2006; Stefan Iglauer et al., 2015; S. Iglauer et al., 2012; Porter et al., 2010) and should be considered an open question for future research.

The data sets were reconstructed using a GSECARS-specific reconstruction algorithm in IDL 8.1 (ITT Visual Information Solutions) (Rivers et al., 2010). Following reconstruction, each voxel in the reconstructed data sets was then segmented into either water, NAPL, or solid phases using an indicator kriging method (Bhattad et al., 2010; Oh & Lindquist, 1999).

Pore-network extraction algorithms (Thompson et al., 2006; Thompson et al., 2008) identified each unique pore along with relevant topological properties (e.g., pore radius, volume, and throat sizes) within the reconstructed data sets. The pore-network extraction algorithm (Thompson et al., 2008) defined pore bodies similarly to the common definition of largest inscribed sphere in a pore space region (Scheidegger, 1958) but, additionally, employed a burn algorithm to associate pore voxels outside of each inscribed sphere to a pore body. The result is that the pores generated by this extraction algorithm are similar to pore units (e.g., Sweijen et al., 2016; Sweijen et al., 2017; Sweijen et al., 2018) as each identified pore body encompasses the entire pore volume between a set of grains as opposed to the pore volume encompassed by the largest

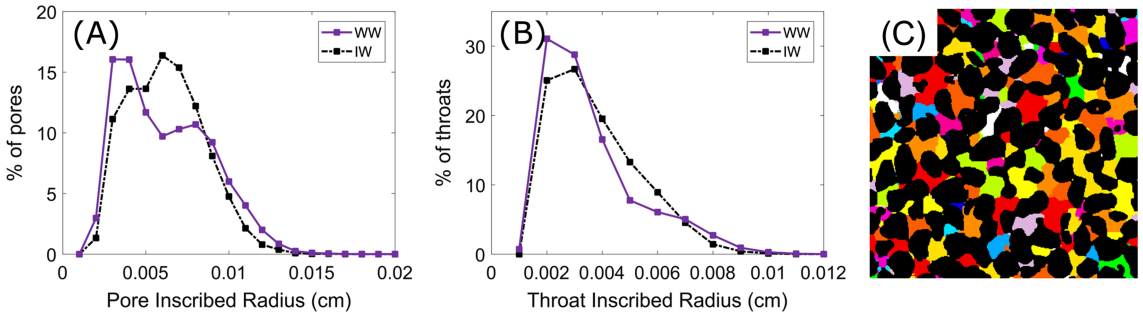

Figure 1. (a) Pore-size distribution by percentage of number of pores, (b) Throat-size distribution by percentage of throats for water wetting (WW, purple) and intermediate wetting sands (IW, black), and (c) A representative slice illustrating pore bodies identified from the pore-network extraction algorithm for the intermediate wetting sand (i.e., quartz sand). Each color represents a single uniquely identified pore body.

inscribed sphere. Throats are also defined in a similar manner to pore units as the facet area between two pore bodies and contain no volume. However, unlike the pore unit generation approach, this algorithm does not rely on assumptions regarding grain packing arrangements (e.g., tetrahedral) or pore body geometry. Figure 1c illustrates the distribution of uniquely identified pore bodies generated by this extraction algorithm from a representative 2-D slice.

The segmented NAPL/water data sets were then mapped onto the extracted pore network to correlate network structure with NAPL/water phase distribution. Previous studies have reported that the ratio of resolution of grain diameter employed within this study is sufficient to accurately quantify and resolve the pore-network structure (Al-Raoush et al., 2003; Al-Raoush & Willson, 2005a, 2005b).

3. Results and Discussion

3.1. Pore-Network Characterization

Table 2 presents an overview of extracted topological and pore-network characteristics. The SXCMT-determined porosities differ between the WW and IW data sets, but otherwise, the pore-network characteristics are generally consistent. Figure 1a illustrates that the distribution of WW and IW pore inscribed radii (PIR) is similar but not identical; the WW sand has a slightly higher percentage of large pores. The higher number of large WW pores corresponds to a higher number of pores with radii between 0.01 and 0.014 cm relative to the IW sand and accounts for the difference in porosity (see Figure S3). Despite differences in pore size distribution, Figure 1b reveals that the distribution of pore throat sizes is almost identical between the two sands.

Given the consistency between the IW and WW pore networks and pore throat size distributions—which control NAPL entry into pore bodies—we have a high degree of confidence in comparing DNAPL distribution between the two networks. Specifically, the analyses presented within this paper focus on whether individual pores are occupied by water or NAPL, the influence of pore size on that phase occupancy, and quantifying NAPL saturation within individual pore bodies. As a result, ensuring that the size and shape characteristics of individual pores are comparable between the two data sets is crucial, and Table 2, Figure 1, and Figure S3 demonstrate that both data sets have a similar number of pores, similar number of throats, and similar pore connectivity's and span the same range of PIR.

Table 2
Overview of Extracted Pore Network and Pore Topological Characteristics

Parameter	WW sand	IW sand
Porosity (%)	41	33
# pores	17,383	17,836
# throats	114,722	102,563
Avg. pore connectivity[a]	6.6	5.7
Avg. PIR[b] (cm)	0.0057	0.0057

[a]The average number of pores connected to a single pore body [b]Pore inscribed radius (PIR) is the radius of the largest sphere that can be drawn within a pore(Thompson et al., 2006).

3.2. Macroscopic NAPL Saturation Trends

Vertical cross sections of the fluid distribution in the 150 μL WW and 200 μL IW data sets are presented in Figure 2a and 2b along with magnified views of a portion of the cross sections in Figure 2c and 2d. Cross-sectional views of all collected WW and IW data sets are presented in Figures S1 and S2, respectively. The two data sets were chosen for comparison as their NAPL invasion fronts reach

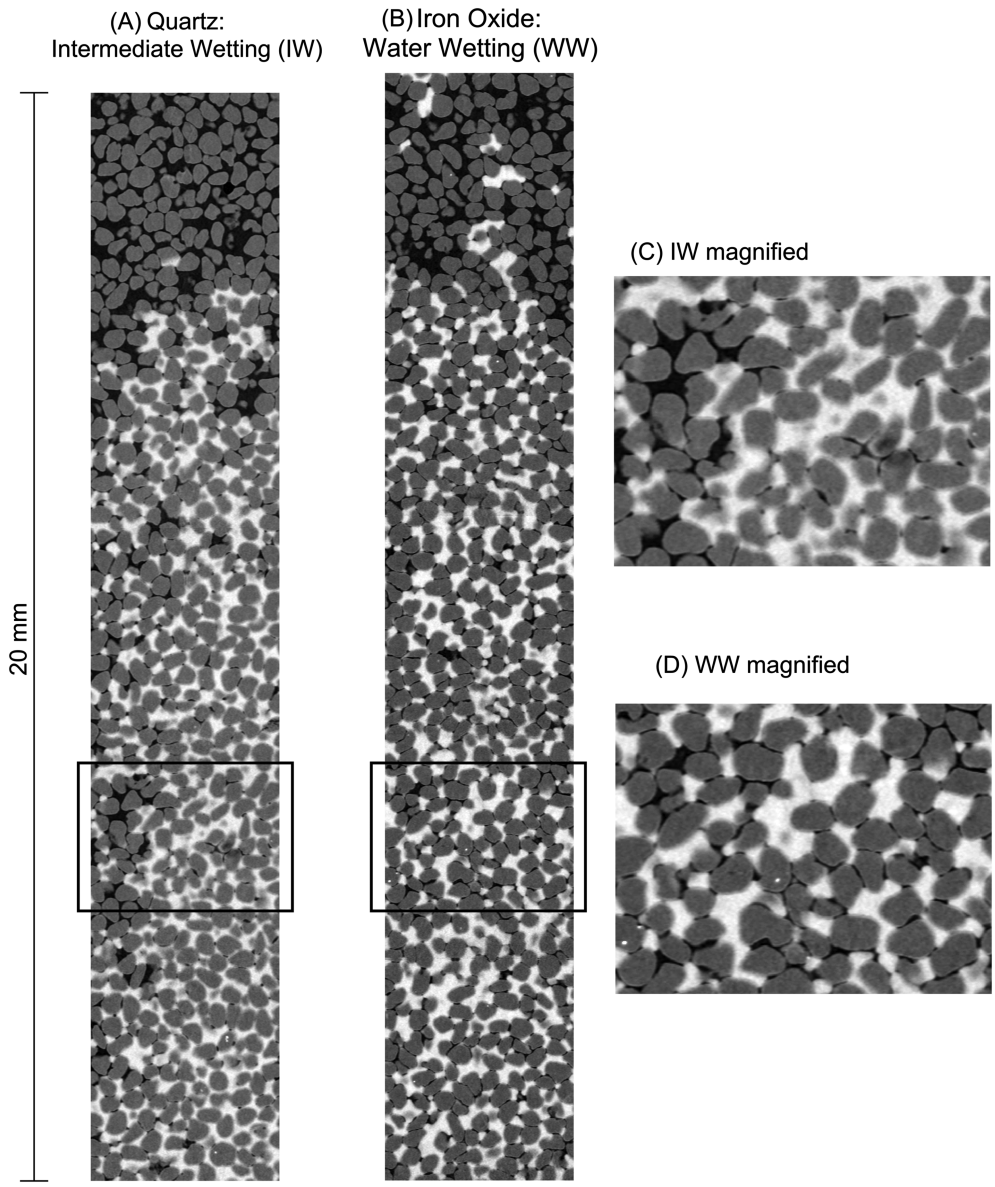

Figure 2. Representative vertical cross sections of (A) intermediate wetting and (B) water wetting systems after injecting 150 and 200 μL of NAPL, respectively. In the images white = NAPL, gray = sand, and black = water. (C) and (D): Magnified views of the outlined sections in images (A) and (B).

approximately the same height in both columns. In Figures 2a and 2b, the injected NAPL was present up to between 1.8 and 1.9 cm from the base of the image.

Within the WW sand, pores appear to contain both NAPL and water, with water remaining in the throats and at grain-grain contacts (Figure 2d). In the IW sand, water residual appears to be in larger, connected ganglia (Figure 2c) with little water in pores that have been invaded by NAPL.

The qualitative observations of residual water structures in Figure 2 are similar to Han et al. (2006) who examined the distribution of residual water structures with XCT and noted larger multipore water ganglia in mixed-wetting systems. Similarly, Al-Menhali et al. (2016) noted that residual CO_2 structures also favored larger, multipore ganglia in mixed-wetting systems. Bench-scale experimental studies of $scCO_2$ trapping have hypothesized the formation of large, multipore residual ganglia in IW systems (e.g., Alyafei & Blunt, 2016); however, this has never been confirmed. They further proposed pore-bypassing as the mechanism

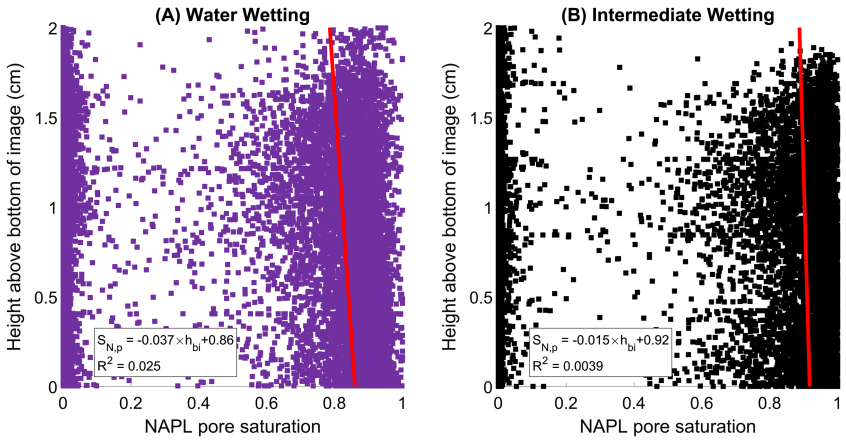

Figure 3. NAPL saturations ($S_{N,p}$) for every individual pore body as a function of each pore's height within the data set (h_{bi}) for the (a) WW and (b) IW systems. Each dot represents 1 pore. Best fit linear trendlines are overlain on each plot alongside the fitted equations describing how $S_{N,p}$ changes with height.

responsible for generating these residual structures. In pore-bypassing, an invading fluid surrounds a cluster of pores occupied by the draining fluid, cutting the draining fluid off from the surrounding pores and generating large multipore residual fluid ganglia. The large water ganglia observed in the IW sand in Figure 2 a and 2c support the hypothesis that IW systems will also form large, multipore structures during drainage.

The relative strength of capillary forces are described using the Capillary (Ca) and Bond (Bo) numbers, defined respectively as the ratios of viscous to capillary and gravity to capillary forces. Ca and Bo values were estimated from equations (1) and (2) (Dawson & Roberts, 1997; Herring et al., 2016):

$$Ca = \frac{v_N \mu_N}{\gamma_{NW} cos\ \theta} \tag{1}$$

$$Bo = \frac{\Delta \rho g d^2}{\gamma_{NW} cos\ \theta} \tag{2}$$

where v_N is the pore water velocity of the injected NAPL, μ_N is the viscosity of the NAPL, γ_{ow} is the interfacial tension of the NAPL-water interface, θ is the contact angle, $\Delta\rho$ is the difference in density between the NAPL and water phases, g is the gravitation constant, and d is the average grain diameter. These relationships are only valid for the contact angle range of $0<|\theta|<90°$. The estimated Ca numbers, using the relationship from Dawson and Roberts (1997), are 6.3×10^{-5} and 2.9×10^{-5} for the IW and WW sands, respectively. The Bo numbers, estimated using a relationship from Herring et al. (2016), are 0.14 and 0.064 for the IW and WW sands, respectively. The differences in Ca and Bo numbers are solely due to the change in wettability. While contact angles were not measured directly within the XCT images, the change in wettability was quantified from the operative contact angles (i.e., contact angles derived by Leverett-scaling capillary pressure-saturation relationships, measured through the water phase) reported in Molnar et al. (2011) as 0° for the WW (iron oxide) sand and 63° for the IW (quartz) sand. These numbers reveal that the IW sand has weaker capillary forces relative to the WW sand.

3.3. Pore Body NAPL Saturation Trends

Piston drainage, the NAPL invasion event that occurs when the system's capillary pressure exceeds the pore body's entry pressure, has been studied both within pore-network modeling (e.g., Blunt, 1998; Blunt et al., 2002; Oren et al., 1998; Oren & Bakke, 2003) and experimentally within complex 3-D media (Berg et al., 2013; Bultreys et al., 2015). This section examines the NAPL saturations within individual pore bodies in the 150 μL WW and 200 μL IW data sets introduced in section 2.1.2.

Figures 3a and 3b plot the measured NAPL pore saturations for each pore in the WW and IW sands as a function of the pore's height from the base of the column. Both columns were identical; images were collected at same distance from the outlet (3 cm from the column outlet) in both WW and IW systems. The observations

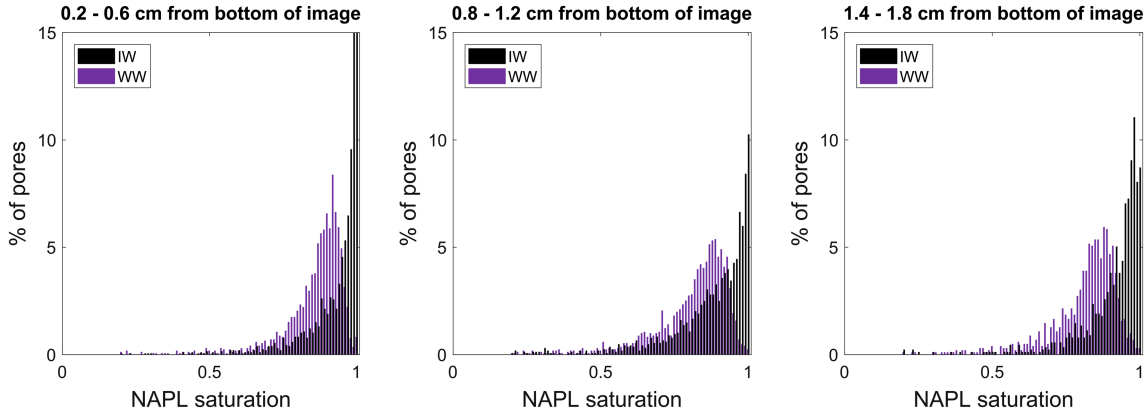

Figure 4. Histograms of pore NAPL saturations for NAPL-occupied pores at selected heights (see Figures 3a and 3b) for the water wetting and intermediate wetting experiments.

are in general agreement with the pore-network modeling predictions that piston drainage generates a minimum NAPL pore saturation. While a range of NAPL pore saturations are observed in both WW and IW sands, most pores either had essentially no NAPL (<0.05) or a high NAPL pore saturation (>0.8). In both WW and IW sands, high NAPL saturations occurred regardless of the pore's location along the NAPL front. Even pores at the very leading edge of the front had high saturations, suggesting that Haines jumps rarely produce pores with low NAPL saturations.

Classical water drainage theory for WW conditions suggests that NAPL pore saturations should increase with capillary pressure as the radius of curvature decreases, allowing water to drain from the corners of the pore (Blunt et al., 2002). Measured NAPL pore saturations within the WW sand (Figure 3a) slowly increase with distance from the leading edge of the NAPL front (i.e., from top to bottom in the column). This agrees with the prediction that pores experience both an initial invasion event followed by the slow, film drainage of water. The measured NAPL pore saturations within the IW sand (Figure 3b) are higher than WW pore saturations at the base of the image (WW: 0.86, IW: 0.92) and change more gradually with distance from the leading edge of the NAPL invasion front (slope of fitted trendlines in Figure 3, WW:−0.037, IW:−0.015). This suggests that while both WW and IW pore bodies experience an initial invasion event, the IW pore saturation changes minimally with higher capillary pressures (i.e., little film drainage occurs).

Pore-network modeling studies of oil-reservoir rocks (e.g., Blunt, 1998; Blunt et al., 2002; Dixit et al., 1996; Dixit et al., 2000; Oren et al., 1998; Oren & Bakke, 2003) typically incorporate wettability changes (i.e., NW or IW systems) using a model proposed by Kovscek et al. (1993). This model suggests that pores are initially water-wet during water drainage (i.e., during the initial Haine's jump). As the NAPL saturation increases within the pore due to film drainage, NAPL will contact the solid surface and change the wettability at that location to either IW or NW, eliminating water films at those contact points. Moreover, this approach predicts an increase in NAPL pore saturation with increasing capillary pressure similar to that predicted (and here observed) for WW sand. However, since Figure 3b illustrates that the NAPL pore saturations change more gradually with height than WW systems, this pore-network modeling approach for draining IW/NW pores is not applicable to the IW system explored in this study. The trends in Figure 3b suggest that the surfactant renders pores IW prior to drainage. This difference between pore-network prediction and experimental observation for IW sand is likely due to the column packing/preparation process employed in this study where the IW sand was initially flushed with surfactant, rendering it IW prior to water drainage.

The differences in NAPL pore saturations between the WW and IW sands are further quantified in Figure 4 for specific regions within the column. While Figures 3a and 3b illustrate how NAPL pore saturations change with distance from the NAPL invasion front (i.e., from top to bottom in the column), Figure 4 directly compares the distribution of NAPL pore saturations between WW and IW wetting conditions. Considering only the pores that contained NAPL (i.e., NAPL pore saturations >0), the NAPL pore saturation distributions exhibit a high degree of skewness, with the highest % of pores at very high NAPL pore saturations. In the IW sand, the highest percentage of NAPL-occupied pores was at NAPL pore saturations of 98%

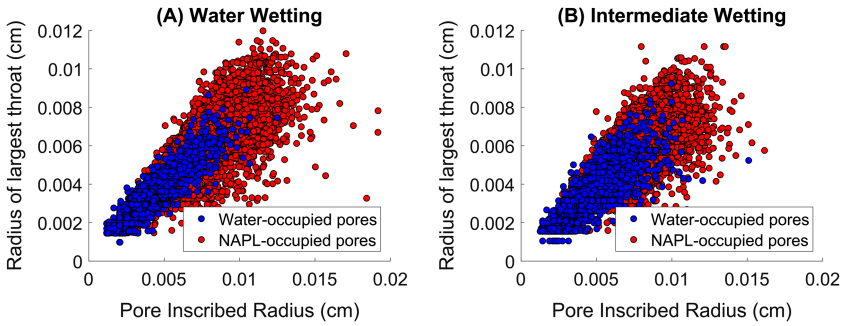

Figure 5. The relationship between a pore body's inscribed radius (*x*-axis) and the radius of the pore's largest throat (*y*-axis) for water wetting (WW, left) and intermediate wetting (IW, right) sands. Each data point represents a single pore body. Blue data points represent water-occupied pores and red data points represent NAPL-occupied pores where NAPL saturation > 20%.

(top), 100% (middle), and 100% (bottom). In the WW sand, the highest percentage of pores had NAPL pore saturations of 88% (top), 89% (middle), and 92% (bottom). This confirms the identified shift toward higher NAPL saturations at greater distances from the NAPL invasion front (and higher capillary pressures) in the WW sand, a trend that is not observed in the IW sand.

The above results generally confirm that NAPL invasion can be treated mainly as a binary event: A pore is either highly saturated with NAPL or water. Few pores possess pore saturations between those extremes. In the IW sand, 16.8% of pores have NAPL pore saturations <0.05, and 74.7% of pores have NAPL pore saturations >0.75, while only 8.5% of pores have saturations in between. Similarly, for the WW sand, 27.5% of pores have NAPL pore saturations <0.05, and 57.9% of pores have NAPL pore saturations >0.75, while only 14.6% of pores have saturations in between.

3.4. Pore Phase Occupancy Trends

Classical water drainage in a uniformly WW sand is expected to first occur in the largest pores (i.e., lowest displacement pressure), followed by medium-sized pores, with the smallest pores either draining last or remaining occupied by residual water (e.g., Blunt, 1998; Blunt et al., 2002; Fenwick & Blunt, 1998; Lenormand et al., 1983; Oren et al., 1998; Oren & Bakke, 2003). This section examines the impact of wettability on this water drainage order by linking phase occupancy of a pore with the characteristics of individual pore bodies for the 150 μL WW and 200 μL IW data sets discussed in sections 2.1.2 and 3.3. For the purpose of this study, a NAPL-occupied pore is defined as any uniquely identified pore that has a NAPL pore saturation greater than 20%. Conversely, a water-occupied pore is defined as a uniquely identified pore with a NAPL saturation less than 20%. Given that few pores possess NAPL pore saturations between 0.05 and 0.75, the saturation threshold chosen to define whether a pore is NAPL- or water-occupied has little impact on any analysis of pore phase occupancy trends.

The following analysis focuses on examining water drainage as a function of pore size. However, in water drainage scenarios, it is throat size, not pore size, that controls the pore's drainage behavior. Due to the complex structure of the two porous media examined in this study and the static nature of time-lapse XCT imaging, it is infeasible to identify which throat controlled the drainage behavior of each pore and assesses pore phase occupancy on that throat's inscribed radii. The analysis presented depends on correlation between pore body size and pore throat size. This correlation is valid for these sands, as demonstrated by Figure 5. It is acknowledged that this may not be the case for all porous media and that this relationship involves some scatter associated with pore structure heterogeneity.

It should be noted that the capillary numbers for WW and IW are outside the range of applicability for percolation theory ($Ca < 10^{-6}$) (Geistlinger et al., 2015). As a result, quantitative predictions from percolation theory (e.g., power-law predictions of residual ganglia size) are not applicable to this study. However, capillary forces still dominate the drainage behavior of both systems, and the classic pore drainage order is still expected. In addition to the macroscopic capillary number discussed in section 2.1.2, the ratio of viscous to capillary forces at the pore scale was calculated utilizing the method of Blunt and Scher (1995) which

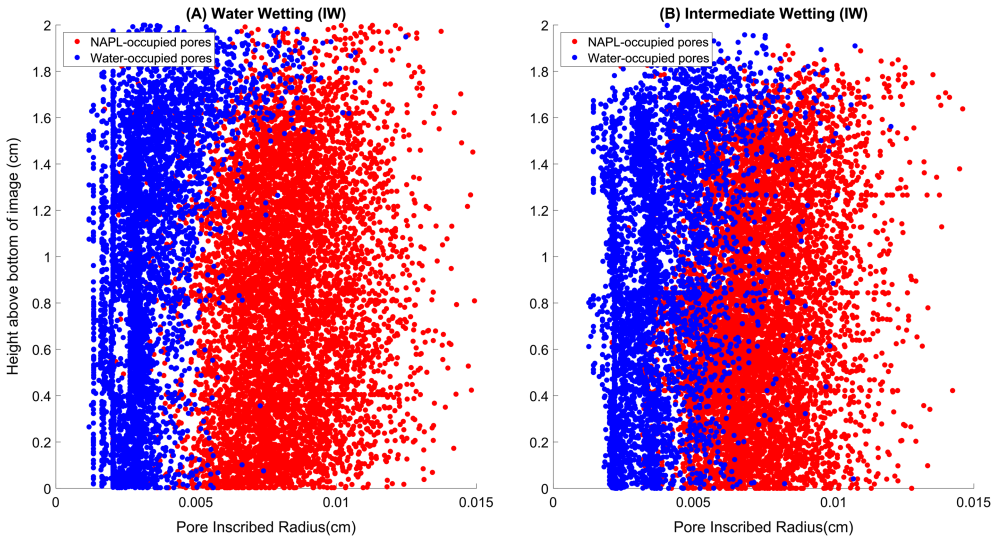

Figure 6. Pore phase occupancy as a function of pore inscribes radii and vertical height for (a) WW and (b) IW sands. Each blue dot represents an individual pore with >80% water saturation. Each red dot represents an individual pore with >20% NAPL saturation. Only water-occupied pores that are immediately adjacent to at least one NAPL-occupied pore are shown.

incorporates throat length (average throat length, WW: 0.28 mm, IW: 0.25 mm) and throat radius (average throat radius, WW: 0.032 mm, IW: 0.030) to yield a viscous/capillary force ratio of 0.03 and 0.05 for the WW and IW systems, respectively. Thus, while pore-scale viscous forces are nonzero in both systems, this force ratio suggests that capillary forces govern pore-scale water drainage. While it is unlikely that the differences in capillary numbers (discussed in section 2.1.2) and pore-scale force balances between the IW and WW sands represent a shift from capillary- to viscous-dominated flow, the following analysis does rely on the assumption that both systems are capillary-force dominated.

The effect of wettability on pore occupancy sequence for the WW and IW sands is presented in Figures 6a and 6b where NAPL- and water-occupied pores are plotted as a function of PIR and height. Only water-occupied pores adjacent to at least one NAPL-occupied pore were included in the figures; therefore, these figures present pores that remained water-occupied due to their geometry rather than simply being far from the NAPL front. In these figures, the bottom region possesses the highest capillary pressures, while the top represents the leading edge of the NAPL invasion front. For this discussion, large pores have PIR > 0.01 cm, medium pores have $0.005 \leq \text{PIR} \leq 0.01$ cm, and small pores have PIR < 0.005 cm. A sensitivity analysis presented in Figure S4 demonstrates that the pore phase occupancy presented in Figures 6a and 6b is insensitive to the chosen NAPL saturation threshold.

The phase occupancy trends observed in Figure 6a for the WW sand confirm the classic water drainage sequence: NAPL first invaded the largest pores (1.4–1.8 cm height) followed by medium-sized pores (0.8–1.2 cm height), and the smallest pores remained water-occupied at all heights. There is a strong separation in Figure 6a between the radii of NAPL-occupied and water-occupied pores. Some deviations from classic water drainage theory exist: 9% of small pores are NAPL-occupied in the WW sand, while ~1% of large pores remained water-occupied. However, the large water-occupied pores were all at the top of the column, suggesting they would eventually be invaded by NAPL. This suggests that pore body radius is a strong, but imperfect, predictor of NAPL invasion in WW porous media.

The predicted drainage order for IW sands is less clear but is expected to be less dependent upon pathway size (i.e., pore size) than WW media (Herring et al., 2016). However, pore-network modeling studies of water drainage in IW systems typically assume a drainage order consistent with percolation theory (i.e., pores with lowest capillary pressure still drain first) (e.g., Blunt, 1998). In IW systems with $\theta < 90^{o}$ (i.e., positive capillary pressures), this assumption predicts a pore drainage order similar to WW systems. However, this assumption has not been tested through observation of 3-D experimental pore-scale systems.

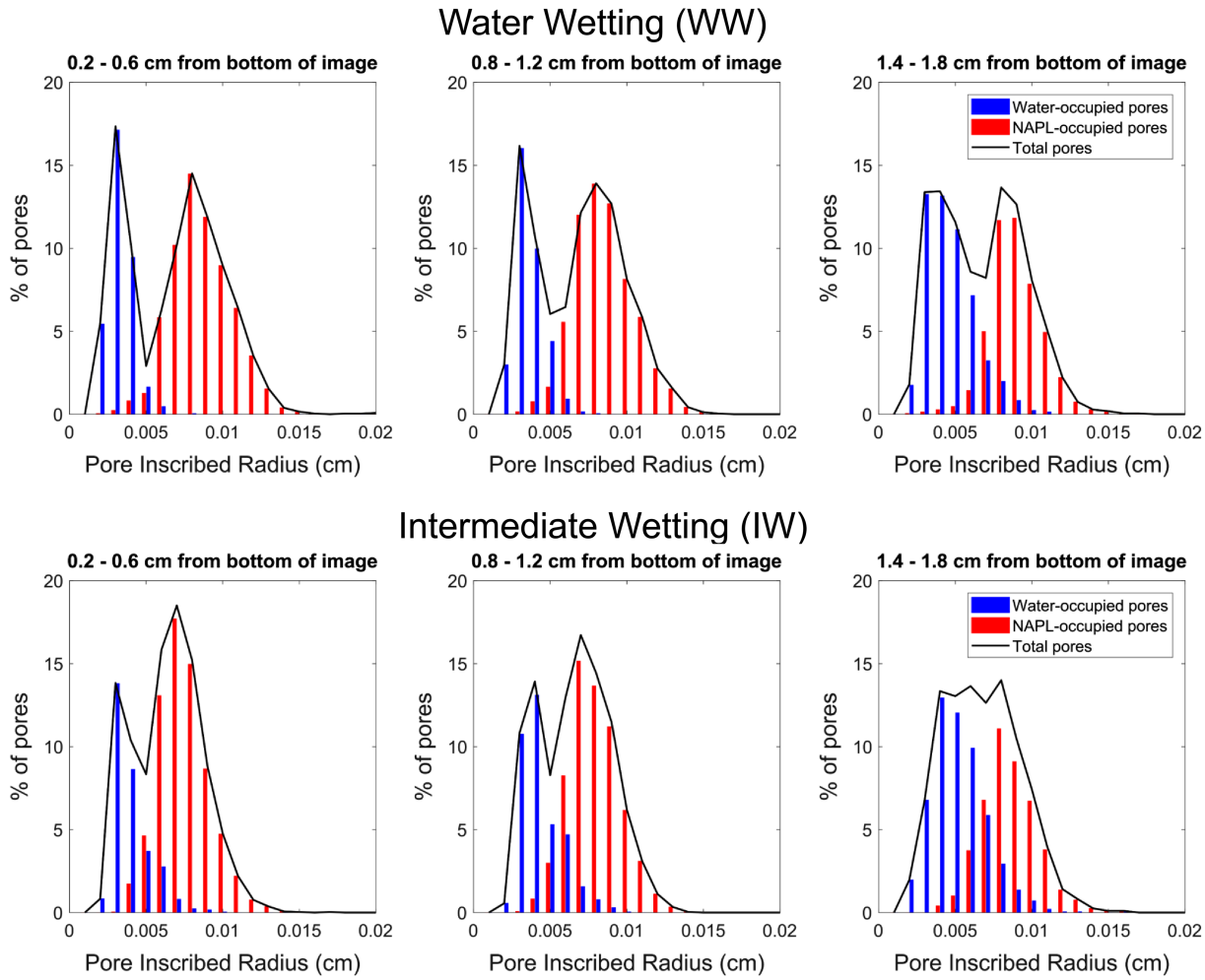

Figure 7. Histograms of pore phase-occupancy versus pore inscribed radii for select height intervals in (a) WW and (b) IW sands. Histograms of the pore inscribed radii for all considered pores (NAPL- + water-occupied pores) are overlain on each height interval (black line).

The IW sand's measured pore occupancy sequence (Figure 6b) illustrates that pore inscribed radius is not as strong a predictor of pore phase occupancy in IW sand as it is in the WW sand. The IW sand's drainage order does not exhibit the strong pore size differentiation between NAPL-occupied and water-occupied pores observed in the WW sand. As in the WW sand, the largest pores are still NAPL-occupied, and the smallest pores are water-occupied. However, a large overlap of NAPL-occupied and water-occupied pore radii exists relative to the WW sand (i.e., more medium-sized pores remained water-occupied). A total of 2% of the large pores with radii >0.01 cm remained water occupied in the IW sand, similar to the WW sand (~1%). However, larger water-occupied pores were observed in the IW sand even near the base of the column where water appears to be at residual macroscopic saturation (Figure 2). As a result, the observed pore occupancy sequence in the IW sand deviates from the expected water drainage order. Figure 6 indicates that NAPL is more likely to bypass medium- and large-sized pores in the IW sand than in the WW sand. This NAPL bypassing phenomenon can be qualitatively observed in the cross-sectional image of the IW sand Figure 2 a. A single, large water ganglion can be seen between 0.4 and 0.8 cm from the bottom of the column.

The wettability induced-deviations from classic water drainage behavior is further quantified in Figure 7 for three distinct regions in the NAPL front: bottom of the column (0.2–0.6 cm from the base), middle of the column (0.8–1.2 cm), and top of the column (1.4–1.8 cm from base). Specifically, Figure 7 presents the percentage of pores occupied by a phase versus inscribed radius of the pore along with the associated total filtered pore size distribution for each specific height interval, while Table 3 summarizes the phase occupancy trends in terms of large, medium, and small pores.

Table 3
Percentage of NAPL-Occupied Pores in WW and IW Sands Sorted by Pore Size

	Large pores (PIR > 0.01 cm)		Medium pores (PIR: 0.005–0.01 cm)		Small pores (PIR < 0.005 cm)	
	WW	IW	WW	IW	WW	IW
Top	98	95	74	65	6.3	4.3
Middle	100	100	98	88	12	13
Bottom	100	100	99	94	9.0	20

Some deviations from the drainage order of large > medium > small pores are expected. Complex pore structures, connectivities, and topology can lead to the drainage of smaller pores with higher entry pressures prior to larger pores, and both percolation theory and pore-network models implicitly account for this (e.g., Blunt et al., 2002). This behavior is observed throughout both WW and IW sands. Within the top region of both WW and IW sands—where capillary pressures are lowest—NAPL occupies a wide range of pore radii (WW: 0.001–0.017 cm, IW: 0.003–0.016 cm) with an overlapping range of water-occupied pore radii (WW: 0.001–0.011 cm, IW: 0.001–0.016 cm). This indicates that NAPL can invade smaller pores prior to larger pores, regardless of the wettability. However, this also illustrates that NAPL bypasses more of the larger water-occupied pores in the IW sand than the WW sand within the top region. This trend extends throughout the data set: NAPL bypassing of medium- and large-sized pores in the IW sand can also be seen in the range of water-occupied pore radii in the middle region (WW: 0.001–0.008 cm, IW: 0.001–0.01 cm) and at the bottom where capillary pressures are the highest (WW: 0.001–0.006 cm, IW: 0.001–0.01 cm).

The similarity of the WW and IW pore-network statistics (e.g., pore and throat size distribution) suggests that these differences in pore occupancy sequence and NAPL bypassing are driven by differences in wettability. For example, in the middle region, 13% of small IW pores are invaded by NAPL before the remaining 12% of medium pores. In contrast, there is little overlap in pore size versus phase occupancy for the WW sand. In the middle region, 12% of small WW pores are invaded with only 2% of medium pores remaining. Examining the top region produces similar conclusions.

The mechanism driving the increased magnitude of NAPL bypassing in the IW sand is not revealed by these data. One potential cause may be that the IW sand became fractionally wetting following preequilibration with the surfactant, instead of achieving a uniform IW condition.

In this study, interactions between the positively charged surfactant (dodecylamine) and mineral surfaces (quartz and iron oxide) controlled the wettability of the system. This rendered the negatively charged quartz surface IW, while the positively charged iron oxide remained WW. A heterogeneous distribution of mineral surface charges and adsorbed surfactant might render the surface fractionally wet. The point of zero charge of the iron oxide sand (6–8) (Molnar et al., 2011) is close to the pH of the system (6.7); thus a heterogeneous distribution of positive and negative surface charges and dodecylamine absorption could be expected. However, the iron oxide system exhibited strongly WW behavior throughout this study, with the classical WW pore occupancy sequence and gradual drainage of water from pore bodies following the initial invasion event, suggesting that it was not fractionally wetted. The point of zero charge of quartz (2) (Molnar et al., 2011) is far from the pH of the system (6.8) and is expected to be predominantly negatively charged, suggesting that fractional wettability could not arise from a variation in surface charges. Mineral heterogeneity on the quartz sand surface, leading to a heterogeneous distribution of surface charges and surfactant adsorption, is also an unlikely cause of fractional wettability as the quartz (IW) sand in this study was a high purity silica sand (Schroth et al., 1996).

Another possibility is that viscous forces are responsible for the deviations from the expected pore drainage order in the IW sand. However, the differences between the viscous/capillary force ratios for the two systems are small (macroscopic-scale capillary numbers: 2.9×10^{-5} versus 6.3×10^{-5} for the WW and IW systems, respectively) relative to the observed differences in pore drainage order. Further work is required to elucidate the mechanisms driving deviations from the expected drainage order in the IW system and should focus on examining IW drainage across a range of capillary and mobility numbers.

An analysis of the total pore size distributions for each height interval in Figure 7 is also unable to explain the bypassing trend. The IW system does have a higher percentage of medium-sized pores (PIR: 0.005–0.01 cm) than the WW system in the top interval. However, the middle and bottom height intervals have comparable pore size distributions between the WW and IW data sets—pore size distributions are generally bi-modal in both WW and IW systems, with peaks occurring at similar inscribed radii values and with similar percentages—and still exhibit bypassing behavior (see Table 3).

The formation of large ganglia in IW scenarios similar to that seen Figure 3a has been observed during drainage from 2-D micromodel cells (e.g., Zhao et al., 2016). It is difficult to compare the bypassing events observed in Figures 5b and 6b to literature observations due to a lack of reported pore sizes and discussion of the phenomena.

A likely explanation for the IW bypassing behavior is the simultaneous existence of concave and convex curvatures across fluid/fluid interfaces that exist in mixed-wetting (Blunt et al., 2019) and uniformly IW (Rabbani et al., 2017; Rabbani et al., 2018) scenarios. In addition, curvatures may flip between concave and convex when interfaces moving through converging and diverging IW pore throats (Rabbani et al., 2018). Thus a range of apparent wettabilities can exist within even uniformly IW media leading to a distribution of positive and negative capillary pressures that changes across time and space. Rabbani et al. (2017) noted the distribution of concave and convex curvatures led to pinned interfaces in scenarios where the interface was expected to advance across a pore body and also to invade fluids withdrawing from already-invaded pores. Such behavior would be expected to lead to the pore-bypassing observed in the IW data sets examined here.

While it is not possible to definitively link the distribution of NAPL/water observed in the IW scenario here to interface curvature dynamics, it does represent the most likely explanation. Developing further understanding of these multipore bypassing events is especially important as they are expected to govern CO_2 trapping in IW systems (Alyafei & Blunt, 2016), increase the rate at which colloids and viruses migrate through the vadose zone (Han et al., 2006), and impact key parameters such as relative permeability which control the rate of NAPL dissolution at contaminated sites (Phelan et al., 2004) and the efficiency of waterflooding for oil recovery (Blunt, 1998).

4. Conclusions

The presented results provide new, direct observations of how WW and IW conditions can affect the pore-scale distribution of NAPL during water drainage. This work addressed several key knowledge gaps (e.g., pore drainage order in weakly WW sands, saturations produced by Haines jumps) with direct experimental pore-scale observations. In so doing, it is now possible to evaluate several hypotheses proposed by pore-scale modeling and bench-scale studies. In several cases, the data confirm existing theories. For example, the data support the fact that capillary forces, relative to viscous and gravity forces, are reduced in IW systems compared to WW systems. Moreover, these observations substantiate that, regardless of wettability, pore-body filling is mainly a binary event (either water- or NAPL-occupied) with few pores exhibiting intermediate NAPL pore saturations.

However, in several areas, the data suggest that existing conceptual models—which have historically focused on water- and NW conditions—do not fully describe the IW scenario examined here and require further development. For example, at the scale of a single pore body, the typical mechanisms of water drainage under WW conditions are generally assumed to be piston displacement followed by film drainage as P_c increases. The NAPL pore saturation distributions quantified in this work support this model for WW systems. For this IW system, these results suggest instead that many residual water structures such as pendular rings, bridges, and water in corners of grain-grain contacts were disrupted by grain-surfactant interactions.

For another example, the standard conceptual model of water drainage suggests that NAPL initially invades the largest pores, followed by increasingly smaller pores as the capillary pressure of the system increases, and this is assumed for both WW and IW systems. The measurements presented here indicate that this drainage order was supported for WW media. However, the IW system examined demonstrated deviations from this standard behavior, increasing the likelihood of NAPL bypassing larger pores, generating multipore water ganglia. The mechanisms governing the observed wettability-induced NAPL distribution may well be due to bypassing mechanisms or coexisting concave and convex NAPL/water interfaces, but this data cannot confirm those related hypotheses.

When pore-phase occupancy and pore-body saturation trends are considered together, the impact of wettability alterations on pore-scale water drainage is not straightforward. There are changes to drainage mechanisms of individual pore bodies as well as changes to the processes occurring at the scale of the pore

network. The changes observed in the IW sand's pore drainage sequence could lead to deviations from pore-network model predictions based upon classic invasion percolation assumptions.

It is acknowledged that our experimental results are discussed in the context of a conceptual understanding of percolation theory. This understanding has emerged from numerous pore-network modeling studies, which rely on numerous assumptions and are generally developed for consolidated porous media. Hence, it may not be entirely fair to compare our results to this understanding so developed. However, this does not alter the fact that our observations are novel and unlike standard expectations.

These results have implications for IW scenarios. The disrupted residual water structures and the corresponding high pore body NAPL saturations will likely increase colloid and virus transport through the vadose zone, as residual water structures are a significant colloid retention mechanism. Similarly, the changes in pore occupancy sequence, especially the increased numbers of water-occupied medium-sized pores, will also increase the mobility of colloids in the vadose zone. NAPL degradation/dissolution processes will be impacted by both the loss of residual water structures within individual pores and the generation of larger multipore water ganglia which will change both the relative permeability and the NAPL-water interfacial area, altering interfacial mass transfer rates. Likewise, the removal of residual water structures during $scCO_2$ injection could eliminate CO_2 snap-off and subsequent capillary trapping during water flushing, leaving the poorly understood process of pore-bypassing and multipore ganglia generation as the predominant trapping mechanisms. In addition, the high pore body saturations in the IW sand could lead to the observed higher pore filling and macroscopic sweep efficiencies for enhanced oil recovery under IW conditions (e.g., Jadhunandan & Morrow, 1995; Kennedy et al., 1955).

The pore-scale observations presented here could be employed to improve descriptions of multiphase flow in both pore-network and continuum models. For instance, incorporating the processes presented here into pore-network models would improve their accuracy for IW scenarios. As relative permeability models, in the absence of experimental data, often rely on data generated by pore-network models, improving the accuracy of pore-network model outputs would improve continuum multiphase flow models. Building the pore-level observations presented here into both pore-network models and conceptual models would improve model descriptions of hysteresis as both pore occupancy sequences and intrapore water distributions following drainage impact imbibition pathways and snap-off/capillary trapping behaviors.

Many of the existing pore-network models developed for IW scenarios rely on the assumption that wettability only changes after water drains from a pore, whereas these results highlight how wettability change can occur before drainage in certain circumstances. Pore-network models would benefit from incorporating this predrainage wetting alteration. Overall, these results point to unique multiphase flow behavior in IW scenarios that should be considered when developing and applying computational models.

It is worth reiterating that these changes were all observed with a relatively small change in operative contact angle, suggesting that only small changes in porous media wettability are needed to influence the water drainage behavior and NAPL distribution, for a wide range of important multiphase systems.

Acknowledgments
We acknowledge the support of GeoSoilEnviroCARS (sector 13), which is supported by the National Science Foundation—Earth Sciences (EAR-1128799) and the Department of Energy—Geosciences (DE-FG02-94ER14466). Use of the Advanced Photon Source, an Office of Science User Facility operated for the U.S. Department of Energy (DOE) Office of Science by Argonne National Laboratory, was supported by the U.S. DOE under contract no. DE-AC02-06CH11357. This research was supported by the Natural Sciences and Engineering Research Council (NSERC) of Canada. Portions of this research (pore-network extraction and image segmentation) were conducted with high-performance computing resources provided by Louisiana State University (http://www.hpc.lsu.edu). The data sets presented within this study can be accessed at the Digital Rocks Portal (https://www.digitalrocksportal.org/).

References

Adler, P. M., & Brenner, H. (1988). Multiphase flow in porous media. *Annual Review of Fluid Mechanics*, *20*(1), 35–59.
Al-Menhali, A. S., & Krevor, S. (2016). Capillary trapping of CO2 in oil reservoirs: Observations in a mixed-wet carbonate rock. *Environmental Science & Technology*, *50*(5), 2727–2734.
Al-Menhali, A. S., Menke, H. P., Blunt, M. J., & Krevor, S. C. (2016). Pore scale observations of trapped CO2 in mixed-wet carbonate rock: Applications to storage in oil fields. *Environmental Science & Technology*, *50*(18), 10282–10290.
Al-Raoush, R. I. (2009). Impact of Wettability on Pore-Scale Characteristics of Residual Nonaqueous Phase Liquids. *Environmental Science & Technology*, *43*(13), 4796–4801.
Al-Raoush, R. I., Abu-Salem, Z., & Willson, C. S. (2003). Characterization of non-wetting phase fluids in porous media systems using high-resolution, three-dimensional, synchrotron X-ray microtomography. *Abstracts of Papers of the American Chemical Society*, *225*, 249. ENVR
Al-Raoush, R. I., & Willson, C. S. (2005a). A pore-scale investigation of a multiphase porous media system. *Journal of Contaminant Hydrology*, *77*(1-2), 67–89.
Al-Raoush, R. I., & Willson, C. S. (2005b). Extraction of physically realistic pore network properties from three-dimensional synchrotron X-ray microtomography images of unconsolidated porous media systems. *Journal of Hydrology*, *300*(1-4), 44–64.
Alyafei, N., & Blunt, M. J. (2016). The effect of wettability on capillary trapping in carbonates. *Advances in Water Resources*, *90*, 36–50.
Anderson, W. (1986a). Wettability literature survey- part 2: Wettability measurement. *Journal of Petroleum Technology*, *38*(11).
Anderson, W. (1986b). Wettability literature survey- part 1: Rock/oil/brine interactions and the effects of core handling on wettability. *Journal of Petroleum Technology*, *38*(10), 1–125.

Anderson, W. G. (1987a). Wettability literature survey part 5: The effects of wettability on relative permeability. *Journal of Petroleum Technology*, *39*(11), 1–453.
Anderson, W. G. (1987b). Wettability literature survey- part 4: Effects of wettability on capillary pressure. *Journal of Petroleum Technology*, *39*(10), 1–283.
Andrew, M., Bijeljic, B., & Blunt, M. (2015). Reservoir condition pore-scale imaging of multiple fluid phases using X-ray microtomography. *Journal of Visualized Experiments: JoVE*, *96*, 52440.
Andrew, M., Bijeljic, B., & Blunt, M. J. (2013). Pore-scale imaging of geological carbon dioxide storage under in situ conditions. *Geophysical Research Letters*, *40*, 3915–3918. https://doi.org/10.1002/grl.50771
Andrew, M., Bijeljic, B., & Blunt, M. J. (2014a). Pore-scale imaging of trapped supercritical carbon dioxide in sandstones and carbonates. *International Journal of Greenhouse Gas Control*, *22*, 1–14.
Andrew, M., Bijeljic, B., & Blunt, M. J. (2014b). Pore-by-pore capillary pressure measurements using X-ray microtomography at reservoir conditions: Curvature, snap-off, and remobilization of residual CO2. *Water Resources Research*, *50*, 8760–8774. https://doi.org/10.1002/2014WR015970
Andrew, M., Bijeljic, B., & Blunt, M. J. (2014c). Pore-scale contact angle measurements at reservoir conditions using X-ray microtomography. *Advances in Water Resources*, *68*, 24–31.
Andrew, M., Menke, H., Blunt, M. J., & Bijeljic, B. (2015). The imaging of dynamic multiphase fluid flow using synchrotron-based X-ray microtomography at reservoir conditions. *Transport in Porous Media*, *110*(1), 1–24.
Arif, M., Al-Yaseri, A. Z., Barifcani, A., Lebedev, M., & Iglauer, S. (2016). Impact of pressure and temperature on CO2–brine–mica contact angles and CO2–brine interfacial tension: Implications for carbon geo-sequestration. *Journal of Colloid and Interface Science*, *462*, 208–215.
Arif, M., Lebedev, M., Barifcani, A., & Iglauer, S. (2017). CO2 storage in carbonates: Wettability of calcite. *International Journal of Greenhouse Gas Control*, *62*, 113–121.
Beatty, S. M., & Smith, J. E. (2010). Fractional wettability and contact angle dynamics in burned water repellent soils. *Journal of Hydrology*, *391*(1), 97–108.
Berg, S., Ott, H., Klapp, S. A., Schwing, A., Neiteler, R., Brussee, N., et al. (2013). Real-time 3D imaging of Haines jumps in porous media flow. *Proceedings of the National Academy of Sciences*, *110*(10), 3755–3759. https://doi.org/10.1073/pnas.1221373110
Berkowitz, B., & Ewing, R. P. (1998). Percolation theory and network modeling applications in soil physics. *Surveys in Geophysics*, *19*(1), 23–72.
Bhattad, P., C. S. Willson, and K. E. Thompson (2010), Segmentation of low-contrast three-phase X-Ray computed tomography images of porous media, paper presented at Proceedings of the GeoX 2010: 3rd International Workshop on X-ray CT for Geomaterials, New Orleans, LA.
Bikkina, P. K. (2011). Contact angle measurements of CO2–water–quartz/calcite systems in the perspective of carbon sequestration. *International Journal of Greenhouse Gas Control*, *5*(5), 1259–1271.
Blunt, M. J. (1998). Physically-based network modeling of multiphase flow in intermediate-wet porous media. *Journal of Petroleum Science and Engineering*, *20*(3), 117–125.
Blunt, M. J., Jackson, M. D., Piri, M., & Valvatne, P. H. (2002). Detailed physics, predictive capabilities and macroscopic consequences for pore-network models of multiphase flow. *Advances in Water Resources*, *25*(8-12), 1069–1089.
Blunt, M. J., Lin, Q., Akai, T., & Bijeljic, B. (2019). A thermodynamically consistent characterization of wettability in porous media using high-resolution imaging. *Journal of Colloid and Interface Science*, *552*, 59–65.
Blunt, M. J., & Scher, H. (1995). Pore-level modeling of wetting. *Physical Review E*, *52*(6), 6387–6403.
Bradford, S. A., & Abriola, L. M. (2001). Dissolution of residual tetrachloroethylene in fractional wettability porous media: Incorporation of interfacial area estimates. *Water Resources Research*, *37*(5), 1183–1195.
Broseta, D., Tonnet, N., & Shah, V. (2012). Are rocks still water-wet in the presence of dense CO2 or H2S? *Geofluids*, *12*(4), 280–294.
Brown, K., Schlüter, S., Sheppard, A., & Wildenschild, D. (2014). On the challenges of measuring interfacial characteristics of three-phase fluid flow with x-ray microtomography. *Journal of Microscopy*, *253*(3), 171–182.
Bultreys, T., Boone, M. A., Boone, M. N., De Schryver, T., Masschaele, B., Van Loo, D., et al. (2015). Real-time visualization of Haines jumps in sandstone with laboratory-based microcomputed tomography. *Water Resources Research*, *51*, 8668–8676. https://doi.org/10.1002/2015WR017502
Chaudhary, K., Bayani Cardenas, M., Wolfe, W. W., Maisano, J. A., Ketcham, R. A., & Bennett, P. C. (2013). Pore-scale trapping of supercritical CO2 and the role of grain wettability and shape. *Geophysical Research Letters*, *40*, 3878–3882. https://doi.org/10.1002/grl.50658
Chiquet, P., Broseta, D., & Thibeau, S. (2007). Wettability alteration of caprock minerals by carbon dioxide. *Geofluids*, *7*(2), 112–122.
Chomsurin, C., & Werth, C. J. (2003). Analysis of pore-scale nonaqueous phase liquid dissolution in etched silicon pore networks. *Water Resources Research*, *39*(9), 1265. https://doi.org/10.1029/2002WR001643
Culligan, K. A., Wildenschild, D., Christensen, B. S. B., Gray, W. G., & Rivers, M. L. (2006). Pore-scale characteristics of multiphase flow in porous media: A comparison of air–water and oil–water experiments. *Advances in Water Resources*, *29*(2), 227–238.
Dawson, H. E., & Roberts, P. V. (1997). Influence of viscous, gravitational, and capillary forces on DNAPL saturation. *Ground Water*, *35*(2), 261–269.
Dixit, A. B., Buckley, J. S., McDougall, S. R., & Sorbie, K. S. (2000). Empirical measures of wettability in porous media and the relationship between them derived from pore-scale modelling. *Transport in Porous Media*, *40*(1), 27–54.
Dixit, A. B., S. R. McDougall, K. S. Sorbie, and J. S. Buckley (1996), Pore scale modelling of wettability effects and their influence on oil recovery, in *SPE/DOE Improved Oil Recovery Symposium*, edited, Society of Petroleum Engineers, Tulsa, Oklahoma.
Fenwick, D. H., & Blunt, M. J. (1998). Three-dimensional modeling of three phase imbibition and drainage. *Advances in Water Resources*, *21*(2), 121–143.
Flury, M., & Qiu, H. (2008). Modeling colloid-facilitated contaminant transport in the Vadose Zone. *Vadose Zone Journal*, *7*(2), 682–697.
Geistlinger, H., & Ataei-Dadavi, I. (2015). Influence of the heterogeneous wettability on capillary trapping in glass-beads monolayers: Comparison between experiments and the invasion percolation theory. *Journal of Colloid and Interface Science*, *459*, 230–240.
Geistlinger, H., Ataei-Dadavi, I., Mohammadian, S., & Vogel, H.-J. (2015). The impact of pore structure and surface roughness on capillary trapping for 2-D and 3-D porous media: Comparison with percolation theory. *Water Resources Research*, *51*, 9094–9111. https://doi.org/10.1002/2015WR017852
Geistlinger, H., & Mohammadian, S. (2015). Capillary trapping mechanism in strongly water wet systems: Comparison between experiment and percolation theory. *Advances in Water Resources*, *79*, 35–50.

Geistlinger, H., Mohammadian, S., Schlueter, S., & Vogel, H.-J. (2014). Quantification of capillary trapping of gas clusters using X-ray microtomography. *Water Resources Research*, *50*, 4514–4529. https://doi.org/10.1002/2013WR014657

Georgiadis, A., Berg, S., Makurat, A., Maitland, G., & Ott, H. (2013). Pore-scale micro-computed-tomography imaging: Nonwetting-phase cluster-size distribution during drainage and imbibition. *Physical Review E*, *88*(3), 033002.

Gershenzon, N. I., Ritzi, R. W., Dominic, D. F., Mehnert, E., & Okwen, R. T. (2017). Capillary trapping of CO2 in heterogeneous reservoirs during the injection period. *International Journal of Greenhouse Gas Control*, *59*(Complete, 13–23.

Haines, W. B. (1930). Studies in the physical properties of soil. V The hysteresis effect in capillary properties, and the modes of moisture distribution associated therewith. *The Journal of Agricultural Science*, *20*(1), 97–116.

Han, J., Jin, Y., & Willson, C. S. (2006). Virus retention and transport in chemically heterogeneous porous media under saturated and unsaturated flow conditions. *Environmental Science & Technology*, *40*(5), 1547–1555.

Heiba, A. A., G. R. Jerauld, H. T. Davis, and L. E. Scriven (1986), Mechanism-based simulation of oil recovery processes, in *SPE Annual Technical Conference and Exhibition*, edited, p. 16, Society of Petroleum Engineers, New Orleans, Louisiana.

Herring, A. L., Andersson, L., Schlüter, S., Sheppard, A., & Wildenschild, D. (2015). Efficiently engineering pore-scale processes: The role of force dominance and topology during nonwetting phase trapping in porous media. *Advances in Water Resources*, *79*, 91–102.

Herring, A. L., Harper, E. J., Andersson, L., Sheppard, A., Bay, B. K., & Wildenschild, D. (2013). Effect of fluid topology on residual non-wetting phase trapping: Implications for geologic CO2 sequestration. *Advances in Water Resources*, *62*, 47–58.

Herring, A. L., Sheppard, A., Andersson, L., & Wildenschild, D. (2016). Impact of wettability alteration on 3D nonwetting phase trapping and transport. *International Journal of Greenhouse Gas Control*, *46*, 175–186.

Holtzman, R., & Segre, E. (2015). Wettability stabilizes fluid invasion into porous media via nonlocal, cooperative pore filling. *Physical Review Letters*, *115*(16), 164501.

Hou, B., Wang, Y., Cao, X., Zhang, J., Song, X., Ding, M., & Chen, W. (2016). Mechanisms of enhanced oil recovery by surfactant-induced wettability alteration. *Journal of Dispersion Science and Technology*, *37*(9), 1259–1267.

Hsu, H.-L., & Demond, A. H. (2007). Influence of organic acid and organic base interactions on interfacial properties in NAPL-water systems. *Environmental Science and Technology*, *41*(3), 897–908.

Iglauer, S., Fernø, M. A., Shearing, P., & Blunt, M. J. (2012). Comparison of residual oil cluster size distribution, morphology and saturation in oil-wet and water-wet sandstone. *Journal of Colloid and Interface Science*, *375*(1), 187–192.

Iglauer, S., Paluszny, A., Pentland, C. H., & Blunt, M. J. (2011). Residual CO2 imaged with X-ray micro-tomography. *Geophysical Research Letters*, *38*, L21403. https://doi.org/10.1029/2011GL049680

Iglauer, S., Pentland, C. H., & Busch, A. (2015). CO2 wettability of seal and reservoir rocks and the implications for carbon geo-sequestration. *Water Resources Research*, *51*, 729–774. https://doi.org/10.1002/2014WR015553

Jadhunandan, P. P., & Morrow, N. R. (1995). Effect of wettability on waterflood recovery for crude-oil/brine/rock systems. *SPE Reservoir Engineering*, *10*(01), 40–46.

Joekar-Niasar, V., & Hassanizadeh, S. M. (2012). Analysis of fundamentals of two-phase flow in porous media using dynamic pore-network models: A review. *Critical Reviews in Environmental Science and Technology*, *42*(18), 1895–1976.

Johnson, P. R., Sun, N., & Elimelech, M. (1996). Colloid transport in geochemically heterogeneous porous media: Modeling and measurements. *Environmental Science & Technology*, *30*(11), 3284–3293.

Kamal, M. S., Hussein, I. A., & Sultan, A. S. (2017). Review on surfactant flooding: Phase behavior, retention, IFT, and field applications. *Energy & Fuels*, *31*(8), 7701–7720.

Kennedy, H. T., Burja, E. O., & Boykin, R. S. (1955). An investigation of the effects of wettability on oil recovery by water flooding. *The Journal of Physical Chemistry*, *59*(9), 867–869.

Kovscek, A. R., Wong, H., & Radke, C. J. (1993). A pore-level scenario for the development of mixed wettability in oil reservoirs. *AICHE Journal*, *39*(6), 1072–1085.

Krevor, S., Blunt, M. J., Benson, S. M., Pentland, C. H., Reynolds, C., Al-Menhali, A., & Niu, B. (2015). Capillary trapping for geologic carbon dioxide storage—from pore scale physics to field scale implications. *International Journal of Greenhouse Gas Control*, *40*, 221–237.

Krevor, S., Pini, R., Zuo, L., & Benson, S. M. (2012). Relative permeability and trapping of CO2 and water in sandstone rocks at reservoir conditions. *Water Resources Research*, *48*, W02532. https://doi.org/10.1029/2011WR010859

Kumar, M., Fogden, A., Senden, T., & Knackstedt, M. A. (2012). Investigation of pore-scale mixed wettability. *SPE Journal*, *17*(1), 20–30.

Kumar, M., Knackstedt, M. A., Senden, T. J., Sheppard, A. P., & Middleton, J. P. (2010). Visualizing and quantifying the residual phase distribution in core material. *Petrophysics*, *51*(5).

Lemke, L. D., & Abriola, L. M. (2006). Modeling dense nonaqueous phase liquid mass removal in nonuniform formations: Linking source-zone architecture and system response. *Geosphere*, *2*(2), 74–82.

Lenormand, R. (1986). Pattern growth and fluid displacements through porous media. *Physica A: Statistical Mechanics and its Applications*, *140*(1), 114–123.

Lenormand, R., Touboul, E., & Zarcone, C. (1988). Numerical models and experiments on immiscible displacements in porous media. *Journal of Fluid Mechanics*, *189*, 165–187.

Lenormand, R., Zarcone, C., & Sarr, A. (1983). Mechanisms of the displacement of one fluid by another in a network of capillary ducts. *Journal of Fluid Mechanics*, *135*, 337–353.

Lord, D. L. (1999), Influence of organic acid and base solution chemistry on interfacial and transport properties of mixed wastes in the subsurface, Ph.D. thesis, 190 pp, University of Michigan, United States -- Michigan.

Melrose, J. C., & Brandner, C. F. (1974). Role of capillary forces in detennining microscopic displacement efficiency for oil recovery by waterflooding. *Journal of Canadian Petroleum Technology*, *13*(4).

Molnar, I. L., O'Carroll, D. M., & Gerhard, J. I. (2011). Impact of surfactant-induced wettability alterations on DNAPL invasion in quartz and iron oxide-coated sand systems. *Journal of Contaminant Hydrology*, *119*(1-4), 1–12.

Morrow, N. R. (1976). Capillary pressure correlations for uniformly wetted porous media. *Journal of Canadian Petroleum Technology*, *15*(4).

Morrow, N. R. (1990). Wettability and its effect on oil recovery. *Journal of Petroleum Technology*, *42*, 1476–1484.

Nambi, I. M., & Powers, S. E. (2000). NAPL dissolution in heterogeneous systems: An experimental investigation in a simple heterogeneous system. *Journal of Contaminant Hydrology*, *44*(2), 161–184.

Norouzi Rad, M., Shokri, N., & Sahimi, M. (2013). Pore-scale dynamics of salt precipitation in drying porous media. *Physical Review E*, *88*(3), 032404.

Oh, W., & Lindquist, W. B. (1999). Image thresholding by indicator kriging. *IEEE Transactions on Pattern Analysis and Machine Intelligence*, *21*(7), 590–602.

Oren, P. E., & Bakke, S. (2003). Reconstruction of Berea sandstone and pore-scale modelling of wettability effects. *Journal of Petroleum Science and Engineering*, *39*(3-4), 177–199.
Oren, P. E., Bakke, S., & Arntzen, O. J. (1998). Extending predictive capabilities to network models. *SPE Journal*, *3*(4), 324–336.
Pentland, C. H., El-Maghraby, R., Iglauer, S., & Blunt, M. J. (2011). Measurements of the capillary trapping of super-critical carbon dioxide in Berea sandstone. *Geophysical Research Letters*, *38*, L0640. https://doi.org/10.1029/2011GL046683
Phelan, T. J., Lemke, L. D., Bradford, S. A., O'Carroll, D. M., & Abriola, L. M. (2004). Influence of textural and wettability variations on predictions of DNAPL persistence and plume development in saturated porous media. *Advances in Water Resources*, *27*(4), 411–427.
Porter, M. L., Wildenschild, D., Grant, G., & Gerhard, J. I. (2010). Measurement and prediction of the relationship between capillary pressure, saturation, and interfacial area in a NAPL-water-glass bead system. *Water Resources Research*, *46*, W08512. https://doi.org/10.1029/2009WR007786
Powers, S. E., Anckner, W. H., & Seacord, T. H. (1996). Wettability of NAPL-contaminated sands. *Journal of Environmental Engineering*, *122*(10), 889–896.
Powers, S. E., Nambi, I. M., & Curry, G. W. (1998). Non–aqueous phase liquid dissolution in heterogeneous systems: Mechanisms and a local equilibrium modeling approach. *Water Resources Research*, *34*(12), 3293–3302.
Rabbani, H. S., Joekar-Niasar, V., Pak, T., & Shokri, N. (2017). New insights on the complex dynamics of two-phase flow in porous media under intermediate-wet conditions. *Scientific Reports*, *7*(1), 4584.
Rabbani, H. S., Zhao, B., Juanes, R., & Shokri, N. (2018). Pore geometry control of apparent wetting in porous media. *Scientific Reports*, *8*(1), 15729.
Rivers, M. L., Citron, D. T., & Wang, Y. B. (2010). Recent developments in computed tomography at GSECARS. In S. R. Stock (Ed.), *Developments in X-Ray Tomography Vii Proc. SPIE 7804, Developments in X-Ray Tomography VII, 780409* (Chap. 780409). Bellingham: Spie-Int Soc Optical Engineering. https://doi.org/10.1117/12.861393
Rücker, M., Berg, S., Armstrong, R. T., Georgiadis, A., Ott, H., Schwing, A., et al. (2015). From connected pathway flow to ganglion dynamics. *Geophysical Research Letters*, *42*, 3888–3894. https://doi.org/10.1002/2015GL064007
Ryder, J. L., & Demond, A. H. (2008). Wettability hysteresis and its implications for DNAPL source zone distribution. *Journal of Contaminant Hydrology*, *102*(1-2), 39–48.
Salathiel, R. A. (1973). Oil recovery by surface film drainage in mixed-wettability rocks. *Journal of Petroleum Technology*, *25*(10), 1–216.
Scheidegger, A. (1958). *The physics of flow through porous media*. London: University Of Toronto Press.
Schnaar, G., & Brusseau, M. L. (2005). Pore-scale characterization of organic immiscible-liquid morphology in natural porous media using synchrotron X-ray microtomography. *Environmental Science & Technology*, *39*(21), 8403–8410.
Schnaar, G., & Brusseau, M. L. (2006). Characterizing pore-scale dissolution of organic immiscible liquid in natural porous media using synchrotron X-ray microtomography. *Environmental Science & Technology*, *40*(21), 6622–6629.
Schroth, M. H., Istok, J. D., Ahearn, S. J., & Selker, J. S. (1996). Characterization of Miller-Similar silica sands for laboratory hydrologic studies. *Soil Science Society of America Journal*, *60*(5), 1331–1339.
Shahraeeni, E., & Or, D. (2010). Pore-scale analysis of evaporation and condensation dynamics in porous media. *Langmuir*, *26*(17), 13924–13936.
Shokri, N., Lehmann, P., & Or, D. (2009). Characteristics of evaporation from partially wettable porous media. *Water Resources Research*, *45*, W02415. https://doi.org/10.1029/2008WR007185
Shokri, N., Lehmann, P., Vontobel, P., & Or, D. (2008). Drying front and water content dynamics during evaporation from sand delineated by neutron radiography. *Water Resources Research*, *44*, W06418. https://doi.org/10.1029/2007WR006385
Singh, K., Bijeljic, B., & Blunt, M. J. (2016). Imaging of oil layers, curvature and contact angle in a mixed-wet and a water-wet carbonate rock. *Water Resources Research*, *52*, 1716–1728. https://doi.org/10.1002/2015WR018072
Sirivithayapakorn, S., & Keller, A. (2003). Transport of colloids in unsaturated porous media: A pore-scale observation of processes during the dissolution of air-water interface. *Water Resources Research*, *39*(12), 1346. https://doi.org/10.1029/2003WR002487
Stauffer, F. (1978), Time dependence of the relations between capillary pressure, water content and conductivity during drainage of porous media, paper presented at IAHR symposium on scale effects in porous media, Thessaloniki, Greece.
Sweijen, T., Aslannejad, H., & Hassanizadeh, S. M. (2017). Capillary pressure–saturation relationships for porous granular materials: Pore morphology method vs. pore unit assembly method. *Advances in Water Resources*, *107*, 22–31.
Sweijen, T., Hassanizadeh, S. M., Chareyre, B., & Zhuang, L. (2018). Dynamic pore-scale model of drainage in granular porous media: The pore-unit assembly method. *Water Resources Research*, *54*, 4193–4213. https://doi.org/10.1029/2017WR021769
Sweijen, T., Nikooee, E., Hassanizadeh, S. M., & Chareyre, B. (2016). The effects of swelling and porosity change on capillarity: DEM coupled with a pore-unit assembly method. *Transport in Porous Media*, *113*(1), 207–226.
Thompson, K. E., Willson, C. S., White, C. D., Nyman, S. L., Bhattacharya, J. P., & Reed, A. H. (2008). Application of a new grain-based reconstruction algorithm to microtomography images for quantitative characterization and flow modeling. *SPE Journal*, *13*(2), 164–176.
Thompson, K. E., Willson, C. S., & Zhang, W. L. (2006). Quantitative computer reconstruction of particulate materials from microtomography images. *Powder Technology*, *163*(3), 169–182.
Ustohal, P., Stauffer, F., & Dracos, T. (1998). Measurement and modeling of hydraulic characteristics of unsaturated porous media with mixed wettability. *Journal of Contaminant Hydrology*, *33*(1), 5–37.
Wan, J., & Tokunaga, T. K. (1997). Film straining of colloids in unsaturated porous media: Conceptual model and experimental testing. *Environmental Science & Technology*, *31*(8), 2413–2420.
Wildenschild, D., Hopmans, J. W., Rivers, M. L., & Kent, A. J. R. (2005). Quantitative analysis of flow processes in a sand using synchrotron-based X-ray microtomography. *Vadose Zone Journal*, *4*(1), 112–126.
Wilkinson, D., & Willemsen, J. F. (1983). Invasion percolation: A new form of percolation theory. *Journal of Physics A: Mathematical and General*, *16*(14), 3365.
Zhao, B., MacMinn, C. W., & Juanes, R. (2016). Wettability control on multiphase flow in patterned microfluidics. *Proceedings of the National Academy of Sciences*, *113*(37), 10,251–10,256.